Growth rate of the turbulent magnetic Rayleigh-Taylor instability

Antoine Briard,* Benoît-Joseph Gréa,† and Florian Nguyen
CEA, DAM, DIF, 91297 Arpajon, France

(Received 27 July 2022; accepted 7 November 2022; published 5 December 2022)

The Rayleigh-Taylor instability is strongly modified in the presence of a vertical mean magnetic field. Perturbations are first stretched in the vertical direction with no mixing due to the inhibition of small-scale shear instabilities. Then smooth elongated fingers eventually break after transition to turbulence, and a strong anisotropy persists. For increasing Alfvèn velocities, the growth rate of the mixing zone in the fully turbulent regime is decreased due to the conversion of potential energy into turbulent magnetic energy. A new theoretical prediction for the growth rate based on turbulent quantities is proposed and assessed with high-resolution direct numerical simulations of the Boussinesq-Navier-Stokes equations under the magnetohydrodynamics approximation.

DOI: 10.1103/PhysRevE.106.065201

I. INTRODUCTION

A perturbed interface between two fluids which is accelerated against the mean density gradient may become unstable due to baroclinic production of vorticity: This is the Rayleigh-Taylor instability (RTI) [1–5]. As the amplitude of the perturbations increases, nonlinear interactions turn the flow into a turbulent mixing zone, which grows at a rate whose determination is of primary importance [6]. Furthermore, if the fluids have magnetic properties, like a turbulent plasma, then the magnetohydrodynamics (MHD) equations have to be used to describe the full dynamics [7].

The magnetic Rayleigh-Taylor instability (MRTI) can play an important role in several industrial and physical applications, in particular inertial confinement fusion (ICF), where hydrodynamic instabilities may cool down the capsule hotspot [8]: In such devices, strong magnetic fluxes might be generated through the Biermann battery effect and hence should be accounted for when designing capsules [9]. In several astrophysical systems, the MRTI is thought to be at the origin of elongated structures, such as in expanding young supernova remnants [10] like the Crab nebula [11], in magnetic fluxes emerging from the Sun interior [12] and in quiescent solar prominences [13]. In particular, the MRTI framework may be used to infer the intensity of the ambient magnetic field from the measure of the exponential growth rate $\sigma = [\mathcal{A}gk_\perp - (\boldsymbol{k}_\perp \cdot \boldsymbol{B}_0)^2]^{1/2}$, with $\boldsymbol{k}_\perp$ the horizontal wave vector of modulus $k_\perp$; $\mathcal{A} = (\rho_1 - \rho_2)/(\rho_1 + \rho_2)$ the Atwood number with ρ_1 and ρ_2 the densities of the heavy and light fluids, respectively; $B_0 = |\boldsymbol{B}_0|$ the mean magnetic field intensity scaled as the Alfvèn velocity; and g the magnitude of the local acceleration [13,14]. However, this method based on the inviscid linear stability analysis [15] may not be adequate for fully turbulent astrophysical objects.

Early simulations, with either a mean magnetic field perpendicular or parallel to the interface, revealed the appearance of elongated structures at onset, and then the dominance of vertical magnetic energy [16]. For three-dimensional simulations of the MRTI with a tangential mean magnetic field, an increase of the growth rate was observed, with large blobs rising due to the reduction of small-scale mixing [17,18]. A different conclusion was obtained in Ref. [19], where a damping of the growth rate was observed when increasing B_0.

This brief survey illustrates that the fate of the MRTI in the fully developed turbulent regime remains unclear. Hence, in this paper, we aim at analyzing the late time dynamics of the MRTI through high-resolution direct numerical simulations (DNS). The main outcome of this study is the derivation of an analytical relation between the growth rate of the mixing zone, the ambient magnetic field intensity, mixing, and anisotropy. This provides a new prediction for the growth rate given the turbulent properties of the flow, which is successfully compared with numerical results.

The magnetic field fluctuations are created by imposing a uniform mean field B_0 oriented perpendicular to the interface, a configuration which preserves statistical axisymmetry, so that models dedicated to the classical RTI can be extended. This particular setup is representative of the interactive outflows of a close-in planet and its host star [20] or of the inner shell of young supernova remnants [10].

II. EQUATIONS AND NUMERICAL SETUP

To assess the effect of a mean magnetic field on the Rayleigh-Taylor instability, we conduct our analysis within the Boussinesq approximation framework, as suggested in Ref. [16]. Then the motion of the two incompressible fluids, initially at rest in an unstable configuration and separated by a perturbed flat interface, is given by the following equations:

$$(\partial_t + \boldsymbol{u}\cdot\nabla - \nu\nabla^2)\boldsymbol{u} = -\nabla(p/\rho_0) - 2\mathcal{A}gC\boldsymbol{n}_3 + (\nabla\times\boldsymbol{B})\times\boldsymbol{B}, \tag{1a}$$

$$(\partial_t + \boldsymbol{u}\cdot\nabla - \eta\nabla^2)\boldsymbol{B} = (\boldsymbol{B}\cdot\nabla)\boldsymbol{u}, \tag{1b}$$

$$(\partial_t + \boldsymbol{u}\cdot\nabla - \kappa\nabla^2)C = 0, \tag{1c}$$

$$\nabla\cdot\boldsymbol{u} = \nabla\cdot\boldsymbol{B} = 0, \tag{1d}$$

*antoine.briard@cea.fr
†benoit-joseph.grea@cea.fr

TABLE I. Parameters of the DNS: number of points, N; Atwood number times acceleration, $\mathcal{A}g$; mean vertical magnetic field intensity, B_0 (scaled as a Alfvèn velocity); diffusion coefficients $\nu = \kappa = \eta$; and final turbulent Reynolds number, Re_t.

N	$\mathcal{A}g$	B_0	ν	$10^{-3} \times \mathrm{Re}_t$
$1024^2 \times 2048$	0.5	[0; 0.02; 0.05; 0.10; 0.15; 0.20; 0.25; 0.30]	2×10^{-4}	[2.1; 2.8; 3.1; 2.5; 2.1; 1.6; 1.5; 1.4]
$1024^2 \times 2048$	1.0	[0; 0.10; 0.20]	2×10^{-4}	[3.3; 4.2; 3.0]
4096^3	0.5	[0; 0.20]	1×10^{-4}	[3.7; 2.5]
4096^3	0.5	[0; 0.20]	5×10^{-5}	[7.7; 5.1]

where $\boldsymbol{u}$ is the velocity field; $\boldsymbol{B} = \boldsymbol{b} + B_0\boldsymbol{n}_3$ the total magnetic field scaled as a velocity, with $\boldsymbol{b}$ the fluctuation and B_0 the mean part along $\boldsymbol{n}_3$ the upward vertical unit vector; p/ρ_0 the reduced pressure with $\rho_0 = (\rho_1 + \rho_2)/2$ the mean density; C the concentration of the heavy fluid related to the density through $\rho/\rho_0 = 1 + 2\mathcal{A}(C - 1/2)$; and ν, η, and κ the constant kinematic viscosity, magnetic diffusivity, and molecular diffusivity, respectively, with here $\nu = \kappa = \eta$.

Here the pseudospectral code `STRATOSPEC` [21] is employed to solve Eqs. (1a)–(1d). The domain is either of size $(2\pi)^3$ for the finest resolutions with 4096^3 points and the smallest diffusion coefficients, or vertically elongated $(2\pi)^2 \times 4\pi$ for the simulations with $1024^2 \times 2048$ points. A classical penalization method is used to ensure periodicity in the vertical inhomogeneous direction, see Ref. [22] for details. A summary of the simulations is provided in Table I, with the values of B_0 indicated in a list for each configuration. The turbulent Reynolds number based on kinetic energy and its dissipation rate is indicated as well at the final time of the simulation: Simulations are stopped when the mixing zone reaches 60% of the domain height. This corresponds to $t = 12$ for the most critical case with $B_0 = 0.3$ in the elongated domain. Larger values of B_0 are not presented since the late-time fully turbulent state is not reached before vertical confinement effects are felt.

The concentration field is set initially with a sharp interface perturbed by small-scale fluctuations of peak wave number $40 \leqslant k_p \leqslant 50$, while the velocity and magnetic fields are zero. Scalar perturbations induce velocity fluctuations through the buoyancy term $2\mathcal{A}gC$ in (1a), which in turn produces magnetic fluctuations through the stretching term $B_0\partial_z\boldsymbol{u}$ in (1b).

III. TRANSITION TO TURBULENCE

When adding a vertical mean magnetic field to the classical RTI configuration, the onset of the instability is slightly delayed compared to the nonmagnetic case in Fig. 1. Still in the early phase from $t = 2$ to $t = 5$, the initial perturbations get more stretched: This was already observed in 2D simulations [16]. The reason is that Kelvin-Helmholtz (KH) shear instabilities at small scales are inhibited by the vertical mean magnetic field. Therefore, mixing is strongly reduced in the early phase, which causes the mixing layer to grow faster. Later at $t = 8$, transition to turbulence has occurred for $B_0 = 0.3$ and mixing between structures has started. At this point, the mixing layer is significantly wider for $B_0 = 0.3$

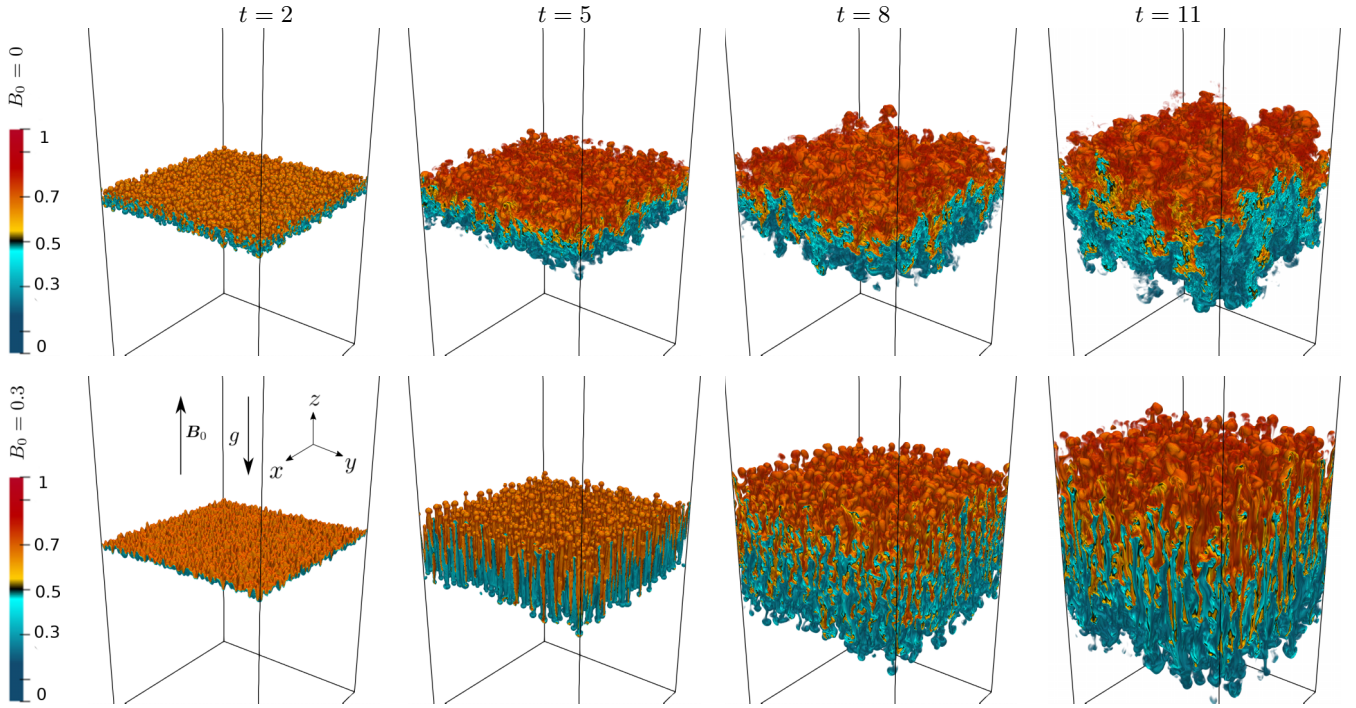

FIG. 1. Time evolution of the concentration field C (pure fluids are transparent) at $t = 2$, 5, 8, and 11 for $B_0 = 0$ (top row) and $B_0 = 0.3$ (bottom row) and for $\mathcal{A}g = 0.5$ in the vertically elongated domain.

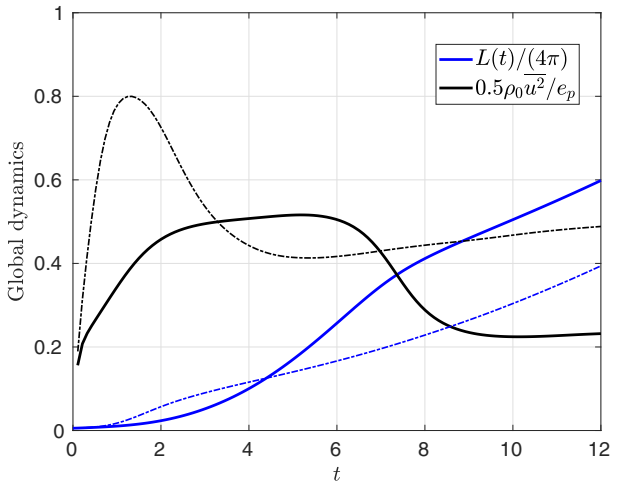

FIG. 2. Mixing zone size L normalized by the domain height (blue) and ratio of kinetic to potential energy $\rho_0\overline{u^2}/(2e_p)$ (black) for $B_0 = 0.3$ (solid line) and $B_0 = 0$ (dash-dotted line) with $\mathcal{A}g = 0.5$ in the vertically elongated domain.

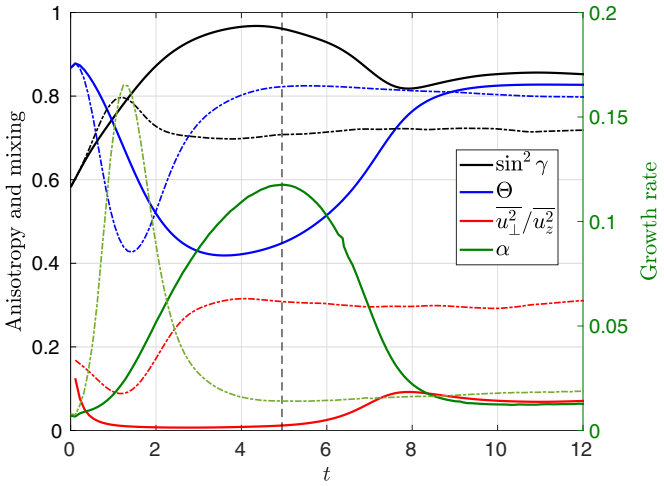

FIG. 3. Mixing parameter Θ (blue), anisotropy of the concentration field $\sin^2\gamma$ (black), anisotropy of the velocity field $\overline{u_\perp^2}/\overline{u_z^2}$ (red), and growth rate α (green) for $B_0 = 0.3$ (solid line) and $B_0 = 0$ (dash-dotted line); the vertical dashed line indicates the time at which $V_z > B_0$.

than $B_0 = 0$. Then, up to $t = 11$, a strong imprint of the mean magnetic field remains, with structures significantly vertically elongated.

This overall dynamics can be quantified using the mixing zone size, defined as [6,23,24]

$$L(t) = 6\int \langle C\rangle(1-\langle C\rangle)dz, \tag{2}$$

where $\langle\star\rangle$ is the horizontal average. This definition is widely used since it provides the exact size for a linear $\langle C\rangle$ profile, which is what is observed in the fully turbulent regime. In Fig. 2, the time evolution of $L(t)$ is presented for the two cases $B_0 = 0$ and $B_0 = 0.3$: One recovers the delayed onset in the presence of the magnetic field, followed by a rapid increase.

The ratio of kinetic to potential energy $\rho_0\overline{u^2}/(2e_p)$ is shown as well, with $\overline{\star} = (1/L)\int\langle\star\rangle dz$ referring to the volume average and where the potential energy is defined with respect to its initial value $e_p = g\overline{z[\rho(0)-\rho]}$, like in Ref. [25]. It is clear that the asymptotic proportion of kinetic energy is strongly reduced for $B_0 = 0.3$ since part of the available potential energy is converted into magnetic energy: This will be discussed further later.

Mixing and anisotropy can be quantified in axisymmetric turbulence using the mixing parameter Θ [3], which tends toward unity for perfectly mixed fluids, and the scalar directional anisotropy parameter $\sin^2\gamma$ [26], which increases from $2/3$ (isotropic value) up to 1 when structures are vertically elongated. Both are defined as

$$\Theta = 1 - \frac{6}{L}\int\langle c^2\rangle dz, \quad \sin^2\gamma = \frac{\int \mathcal{E}_{cc}(\boldsymbol{k})\sin^2\theta d^3V}{\int \mathcal{E}_{cc}(\boldsymbol{k})d^3V}, \tag{3}$$

with $\mathcal{E}_{cc}$ the spectral concentration variance density, θ the angle between $\boldsymbol{k}$ and $\boldsymbol{n}_3$, d^3V the integration volume in spherical coordinates, and $c = C - \langle C\rangle$ the fluctuation.

The time evolution of Θ and $\sin^2\gamma$ is shown in Fig. 3 for $B_0 = 0.3$ compared with the reference case $B_0 = 0$. The directionality parameter $\sin^2\gamma$ first increases, reflecting the stretching in the vertical direction, and then reaches a maximum, much larger for $B_0 = 0.3$, and afterwards decreases with turbulent mixing. One readily observes that the transition to turbulence is strongly delayed in the presence of a mean magnetic field. It is well indicated by the inviscid stability criterion $V_z > B_0$ for KH, which consistently corresponds to the decrease of $\sin^2\gamma$: Here $V_z = (\overline{u_z^2})^{1/2}$ is the typical vertical turbulent velocity.

At the same time, the mixing parameter Θ diminishes because structures are initially stretched without mixing and then increases after transition to turbulence. An unexpected outcome is that the final value of Θ is slightly larger for $B_0 = 0.3$ than $B_0 = 0$, showing somehow that mixing could be more efficient with a mean magnetic field: This is due to the much larger surface available for mixing at the transition to turbulence in the MRTI since structures are vertically elongated.

Finally, the ratio of horizontal to vertical kinetic energy $\overline{u_\perp^2}/\overline{u_z^2}$ also shows the strong anisotropy of the velocity field, since it is three times lower for $B_0 = 0.3$ than for the nonmagnetic case: Hence, even in the fully turbulent regime, there remains a strong imprint of the magnetic field that maintains the flow around field lines.

IV. GROWTH RATE

It is clear from the observations in Fig. 3 that an asymptotic state is eventually reached for the MRTI. In the self-similar regime of the RTI, the mixing zone size evolves as [3]

$$L(t) = 2\alpha\mathcal{A}gt^2, \quad \alpha = \frac{\dot{L}^2}{8\mathcal{A}gL}. \tag{4}$$

The time evolution of the turbulent mixing zone growth rate α is shown in Fig. 3 for $B_0 = 0$ and $B_0 = 0.3$: It decreases after

transition to turbulence to a final value which is lower in the presence of a mean vertical magnetic field. For this particular case ($B_0 = 0.3$, $\nu = 2 \times 10^{-4}$), we obtain a 33% reduction of the growth rate.

In Ref. [26], based on the rapid acceleration (RA) model, a relation was derived between the growth rate and the mixing and anisotropy parameters,

$$\alpha_{\rm hyd} = \frac{\sin^4\gamma(1-\Theta)^2}{1+\sin^2\gamma(1-\Theta)}. \tag{5}$$

This result has proven to be accurate in nonmagnetic configurations [24] and was later extended to second-order correlations in Ref. [27]. In the MRTI, for strong-enough mean magnetic fields, the growth rate is permanently reduced so that the prediction $\alpha_{\rm hyd}$ over-estimates the measured growth rate (see Fig. 5). Moreover, for a given Alfvèn velocity, α is even more reduced when turbulence intensity is increased: This is confirmed by the high-resolution DNS for which the diffusion coefficients are decreased from 2×10^{-4} to 5×10^{-5}.

What is the missing ingredient to more accurately predict the growth rate in the MRTI? Within the RA approach for the classical RTI, a simplified system of equations describing the large-scale dynamics is obtained, which yields a buoyancy-drag equation [28,29]

$$\ddot{L} = -C_d\frac{\dot{L}^2}{L} + C_b\mathcal{A}g, \tag{6}$$

where the buoyancy coefficient is $C_b = 4(1-\Theta)\sin^2\gamma$ and $C_d = 1/2$. Moreover, it can be shown that turbulent dissipation does not modify C_b and only acts as a supplementary drag, which takes the form $C_d = 1/2 + \mathcal{D}$, where $\mathcal{D}$ needs to be modelled [30]. Further using the closure $C_d = 2/C_b$ demonstrated in Ref. [31] in the nonmagnetic case, one recovers (5) in the RA approach, with $\alpha = C_b/(4+8C_d)$ coming from (4) and (6). Thus, our previous question amounts to determine how to modify C_b and C_d to account for the presence of a vertical mean magnetic field.

In the MHD framework, new couplings and correlations come into play so that the RA approach must be adapted. We first define the various spectral densities as $\mathcal{E}_{\beta\gamma}(\boldsymbol{k})\delta(\boldsymbol{k}-\boldsymbol{p}) = \hat{\beta}(-\boldsymbol{p})\hat{\gamma}(\boldsymbol{k})$, where $\hat{\star}$ is the Fourier transform, and with namely the vertical kinetic energy $\mathcal{E}_{uu}$, the vertical magnetic energy $\mathcal{E}_{bb}$, the vertical flux $\mathcal{E}_{uc}$, the scalar variance $\mathcal{E}_{cc}$, the cross-helicity $\mathcal{E}_{ub}$, and the mixed flux $\mathcal{E}_{bc}$. When considering the large scales of these quantities, nonlinear and dissipative terms can be discarded, so that the evolution equations read

$$\frac{\partial\mathcal{E}_{uu}}{\partial t} = -4\mathcal{A}g\sin^2\theta{\rm Re}[\mathcal{E}_{uc}] - 2k\cos\theta B_0{\rm Im}[\mathcal{E}_{ub}], \tag{7a}$$

$$\frac{\partial\mathcal{E}_{bb}}{\partial t} = 2k\cos\theta B_0{\rm Im}[\mathcal{E}_{ub}], \tag{7b}$$

$$\frac{\partial\mathcal{E}_{cc}}{\partial t} = -\frac{2}{L}{\rm Re}[\mathcal{E}_{uc}], \tag{7c}$$

$$\frac{\partial\mathcal{E}_{uc}}{\partial t} = -2\mathcal{A}g\sin^2\theta\mathcal{E}_{cc} - \frac{1}{L}\mathcal{E}_{uu} - ik\cos\theta B_0\mathcal{E}_{bc}. \tag{7d}$$

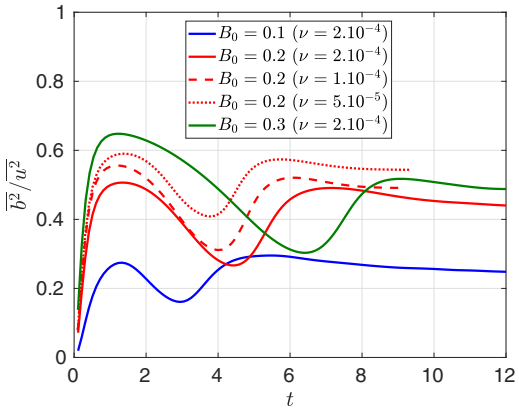

FIG. 4. Magnetic to kinetic energy ratio $\overline{b^2}/\overline{u^2}$ as function of time for various Alfvèn velocities B_0 and diffusion coefficients ν.

Interestingly, Eqs. (7a)–(7d) describing the large-scales dynamics of the MRTI reduce for $\theta = \pi/2$ to the hydrodynamics RA equations for $\theta = \pi/2$, with no explicit magnetic contributions. However, fluctuations are the most amplified and contribute dominantly to the overall dynamics for this particular angle [26,27]: This means that magnetic effects play a role through nonlinear interactions between different angles and scales, which are now taken into account by spherically averaging the system (7). Further summing (7a)–(7b) cancels out the redistribution term associated to $\mathcal{E}_{ub}$, yielding

$$\frac{\partial}{\partial t}(E_{uu}+E_{bb}) = -4\mathcal{A}g\int\mathcal{E}_{uc}\sin^2\theta\, d^2S_k, \tag{8a}$$

$$\frac{\partial E_{uc}}{\partial t} = -2\mathcal{A}g\int\mathcal{E}_{cc}\sin^2\theta\, d^2S_k - \frac{E_{uu}}{L} - iB_0\int k\mathcal{E}_{bc}\cos\theta\, d^2S_k, \tag{8b}$$

$$\frac{\partial E_{cc}}{\partial t} = -\frac{2}{L}E_{uc}, \tag{8c}$$

where the spherically averaged spectrum is $E_{\beta\gamma}(k) = \int\mathcal{E}_{\beta\gamma}(\boldsymbol{k})d^2S_k$, with $d^2S_k = k^2\sin\theta d\theta d\phi$ the surface integration at constant k.

To close the system (8), we finally make two assumptions. (i) We consider only the leading θ contributions, namely $\theta \to \pi/2$, which amounts to discard the $\mathcal{E}_{bc}$ term (this is further assessed by numerical results which indicate that $\overline{b_z c}$ is orders of magnitude smaller than $\overline{u_z^2}$ and $\overline{c^2}$). (ii) We assume a constant ratio $R = E_{bb}/E_{uu}$ at large scales in the self-similar regime. By doing so, we consider that most of the energy is contained in the largest scales; but R also reflects how the nonlinear interactions at smaller scales impact the largest ones. This assumption is justified in Fig. 4 by the fact that the magnetic-to-kinetic energy ratio $\overline{b^2}/\overline{u^2} \simeq \overline{b_z^2}/\overline{u_z^2}$ eventually tends to a constant, which increases with B_0 and the turbulent intensity. Here one relates spectra and energies through $L\overline{u_z^2} = L_z\int E_{uu}\,dk$ and $L\overline{b_z^2} = L_z\int E_{bb}\,dk$, where L_z is the domain height.

Hence, the final simplified system describing the large-scale dynamics of the MRTI is

$$(1+R)\frac{\partial E_{uu}}{\partial t} = -4\mathcal{A}gE_{uc}, \tag{9a}$$

$$\frac{\partial E_{uc}}{\partial t} = -2\mathcal{A}gE_{cc} - \frac{E_{uu}}{L}, \tag{9b}$$

$$\frac{\partial E_{cc}}{\partial t} = -\frac{2}{L}E_{uc}. \tag{9c}$$

Coming back to the system (8), it is possible to derive a new buoyancy-drag equation in the context of the MRTI. Using the approximation $E_{bb} = RE_{uu}$, and performing an expansion of the spectra in Legendre polynomials like in Ref. [26], one eventually gets

$$\ddot{L} = -\underbrace{\left(\frac{1}{2}+\frac{R}{2R+3}\right)}_{C_d}\frac{\dot{L}^2}{L} + \underbrace{4\sin^2\gamma(1-\Theta)}_{C_b}\mathcal{A}g, \tag{10}$$

where $C_d = (1/2) + R/(2R+3)$ is the new drag coefficient in the presence of a normal mean magnetic field (for $R = 0$, one recovers the result of the classical RTI). Since $R > 0$ in the MRTI, this analysis shows that only the drag coefficient is increased in the presence of turbulent magnetic energy, thus reducing the growth rate, while the buoyancy coefficient is left unchanged. Still, this expression for C_d is not predictive since turbulent dissipation has to be taken into account: Hence, a new closure for the drag coefficient needs to be derived.

To do so, we finally assume self-similarity of the large scales, like in Ref. [31]: The various spectra read $E_{\beta\gamma} = E^0_{\beta\gamma}k^s t^{n_{\beta\gamma}}$, with the amplitudes $E^0_{\beta\gamma}$ and the exponents $n_{\beta\gamma}$ and s independent of space and time: Note that due to the production terms in the system (9), all three spectra have the same infrared slope s. Further using the previous outcome that only the drag coefficient C_d is increased by R, this gives the following closure for the drag coefficient in the MRTI, $C_d = 2(1+R)/C_b + R/2$, which consistently reduces to $C_d = 2/C_b$ in the hydrodynamic case [31]. This yields a new relation between the growth rate of the mixing zone in the magnetic Rayleigh-Taylor instability and the turbulent quantities

$$\alpha_{\mathrm{MHD}} = \frac{\sin^4\gamma(1-\Theta)^2}{(1+R)[1+\sin^2\gamma(1-\Theta)]} = \frac{\alpha_{\mathrm{hyd}}}{1+R}. \tag{11}$$

Hence, the presence of magnetic energy reduces the growth rate, and R can be as large as 55% in Fig. 4.

This new prediction is confronted to all the simulations of Table I in Fig. 5. The α evaluated from the DNS (black squares) are averaged over the two last times. It is clear that the results in the hydrodynamic case (blue circles) given by (5) always overestimate the true value of α when the mean magnetic field B_0 increases. On the contrary, the present relation (11) accounting for the magnetic energy (red crosses) is much closer to the DNS results, with excellent agreement for the largest B_0. One may argue that for the lowest Alfvèn velocities, namely $B_0 \leqslant 0.1$, the magnetic energy spectra are not developed enough so that the assumptions of self-similarity and constant ratio R are questionable; still, it provides better results than the nonmagnetic prediction.

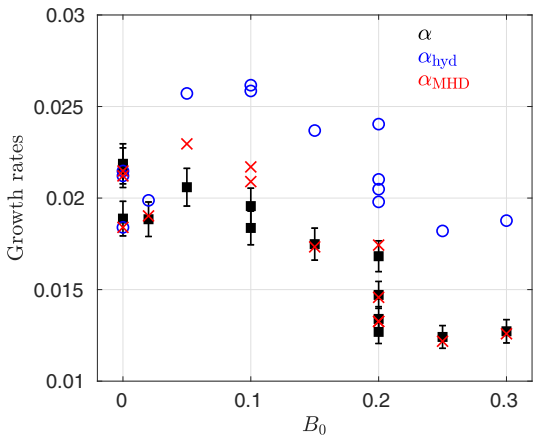

FIG. 5. Growth rates of the mixing zone for the DNS of Table I as function of B_0. [□ (black)] numerical result averaged over the two last times with ±5% error bar; [○ (blue)] hydrodynamic prediction (5); [× (red)] MHD prediction (11).

V. APPLICATIONS AND CONCLUSIONS

To interpret observational data, the relation (11) can be used to estimate the ambient magnetic field intensity $b_0 = \sqrt{\overline{b^2}}$ through $b_0 = u_0\sqrt{\alpha_{\mathrm{hyd}}/\alpha - 1}$. One also needs an estimation for $u_0 = \sqrt{\overline{u^2}}$ from direct measurements. Then α_{hyd} depends only on the mixing and anisotropy parameters, as given by (5): Typical values can be chosen, such as $\Theta \simeq 0.8$ and $0.8 \leqslant \sin^2\gamma \leqslant 0.9$. Finally, the actual growth rate α of the mixing zone is required: Unfortunately, this is rarely provided, since the exponential growth rate coming from the linear stability analysis is often used [14,32]. Still, α could be evaluated using the self-similar expression (4) from visualizations at two different instants if the heights of the structures were systematically reported.

In Ref. [14], solar limb prominences are analyzed, but the data reported are not sufficient to evaluate α. Nevertheless, we can comment on the observations regarding the occurrence of November 2006 in Fig. 11 of Ref. [14]. Elongated structures are clearly visible: However, the typical transverse length scale between two structures significantly increases between two instants, which is the signature of strong nonlinear mechanisms, which thus possibly discards analysis relying solely on the linear stability.

As a conclusion, the overall dynamics of the Rayleigh-Taylor instability is significantly impacted by the presence of magnetic energy, created here through a vertical mean field. First, the transient regime exhibits strong anisotropy with a rapid stretching of the structures, which then break at transition to turbulence, yielding an enhanced mixing. Hence, the fully turbulent state is significantly altered, with a reduced growth rate of the mixing zone, since part of the potential energy is converted into magnetic energy rather than kinetic energy. This reduction is remarkably captured by an adaptation of the rapid acceleration model to the MHD framework. The new prediction derived here for the mixing zone growth rate can be used to adapt turbulent models for ICF and to infer local magnetic field intensities in turbulent astrophysical configurations.

ACKNOWLEDGMENT

The simulations were performed at the French computing facility CEA HF.

[1] L. Rayleigh, Investigation of the character of the equilibrium of an incompressible heavy fluid of variable density, Proc. Lond. Math. Soc. **s1-14**, 170 (1882).

[2] G. Taylor, The instability of liquid surfaces when accelerated in a direction perpendicular to their planes, Proc. R. Soc. Lond. **192**, 201 (1950).

[3] D. Youngs, Numerical simulation of mixing by Rayleigh-Taylor and Richtmyer-Meshkov instabilities, Laser Part. Beams **12**, 725 (1994).

[4] W. Cabot and A. Cook, Reynolds number effects on Rayleigh-Taylor instability with possible implications for type-ia supernovae, Nat. Phys. **2**, 562 (2006).

[5] Y. Zhou, Rayleigh-Taylor and Richtmyer-Meshkov instability induced flow, turbulence and mixing i, Phys. Rep. **720-722**, 1 (2017).

[6] G. Dimonte *et al.*, A comparative study of the turbulent Rayleigh-Taylor instability using high-resolution three-dimensional numerical simulations: The Alpha-Group collaboration, Phys. Fluids **16**, 1668 (2004).

[7] D. Biskamp, *Magnetohydrodynamic Turbulence* (Cambridge University Press, Cambridge, UK, 2003)

[8] B. Remington *et al.*, Rayleigh-Taylor instabilities in high-energy density settings on the National Ignition Facility, Proc. Natl. Acad. Sci. USA **116**, 18233 (2019).

[9] C. Walsh and D. Clark, Biermann battery magnetic fields in ICF capsules: Total magnetic flux generation, Phys. Plasmas **28**, 092705 (2021).

[10] B.-I. Jun and M. Norman, On the origin of radial magnetic fields in young supernova remnants, Astrophys. J. **472**, 245 (1996).

[11] C. Cox, S. Gull, and D. Green, Numerical simulations of the 'jet' in the Crab Nebula, Mon. Not. R. Astron. Soc. **250**, 750 (1991).

[12] H. Isobe, T. Miyagoshi, K. Shibata, and T. Yokoyama, Filamentary structure on the Sun from the magnetic Rayleigh–Taylor instability, Nature (Lond.) **434**, 478 (2005).

[13] A. Hillier, The magnetic Rayleigh-Taylor instability in solar prominences, Rev. Mod. Plasma Phys. **2**, 1 (2018).

[14] M. Ryutova, T. Berger, Z. Frank, T. Tarbell, and A. Title, Observation of plasma instabilities in quiescent prominences, Sol. Phys. **267**, 75 (2010).

[15] S. Chandrasekhar, in *Hydrodynamic and Hydromagnetic Stability* (Oxford University Press, Oxford, UK, 1961), Chap. 10, pp. 429–480

[16] B.-I. Jun, M. Norman, and J. Stone, The non-linear growth of the magnetic Rayleigh-Taylor instability, Astrophys. J. **453**, 332 (1995).

[17] J. Stone and T. Gardiner, The magnetic Rayleigh-Taylor instability in three dimensions, Astrophys. J. **671**, 1726 (2007).

[18] J. Stone and T. Gardiner, Nonlinear evolution of the magnetohydrodynamic Rayleigh-Taylor instability, Phys. Fluids **19**, 094104 (2007).

[19] J. Carlyle and A. Hillier, The non-linear growth of the magnetic Rayleigh-Taylor instability, Astron. Astrophys. **605**, A101 (2017).

[20] T. Matsakos, A. Uribe, and A. Königl, Classification of magnetized star-planet interactions: Bow shocks, tails, and inspiraling flows, Astron. Astrophys. **578**, A6 (2015).

[21] G. Viciconte, B.-J. Gréa, F. S. Godeferd, P. Arnault, and J. Cléroin, Sudden diffusion of turbulent mixing layers in weakly coupled plasmas under compression, Phys. Rev. E **100**, 063205 (2019).

[22] A. Briard, L. Gostiaux, and B.-J. Gréa, The turbulent Faraday instability in miscible fluids, J. Fluid Mech. **883**, A57 (2020).

[23] M. Andrews and D. Spalding, A simple experiment to investigate two-dimensional mixing by rayleigh-taylor instability, Phys. Fluids A **2**, 922 (1990).

[24] B. Morgan and W. Black, Parametric investigation of the transition to turbulence in Rayleigh-Taylor mixing, Physica D **402**, 132223 (2020).

[25] A. Cook, W. Cabot, and P. Miller, The mixing transition in Rayleigh-Taylor instability, J. Fluid Mech. **511**, 333 (1999).

[26] B.-J. Gréa, The rapid acceleration model and the growth rate of a turbulent mixing zone induced by Rayleigh-Taylor instability, Phys. Fluids **25**, 015118 (2013).

[27] O. Soulard, J. Griffond, and B.-J. Gréa, Influence of the mixing parameter on the second-order moments of velocity and concentration in Rayleigh-Taylor turbulence, Phys. Fluids **28**, 065107 (2016).

[28] R. Davies and G. Taylor, The mechanics of large bubbles rising through extended liquids and through liquids in tubes, Proc. R. Soc. Lond. **200**, 375 (1950).

[29] G. Dimonte, Spanwise homogeneous buoyancy-drag model for Rayleigh-Taylor mixing and experimental evaluation, Phys. Plasma **7**, 2255 (2000).

[30] J. D. Ramshaw, Simple model for linear and nonlinear mixing at unstable fluid interfaces with variable acceleration, Phys. Rev. E **58**, 5834 (1998).

[31] O. Poujade and M. Peybernes, Growth rate of Rayleigh-Taylor turbulent mixing layers with the foliation approach, Phys. Rev. E **81**, 016316 (2010).

[32] J. Carlyle, D. Williams, L. van Driel-Gesztelyi, D. Innes, A. Hillier, and S. Matthews, Investigating the dynamics and density evolution of returning plasma blobs from the 2011 June 7 eruption, Astrophys. J. **782**, 87 (2014).